GEOPHYSICS, VOL. 74, NO. 5 (SEPTEMBER-OCTOBER 2009); P. N31–N39, 6 FIGS.
10.1190/1.3192911

Theory and numerical simulation of fluid-pressure diffusion in anisotropic porous media

José M. Carcione[1] and Davide Gei[1]

ABSTRACT

The physics of fluid diffusion in anisotropic media was studied, based on Biot's theory of poroelasticity and using wave propagation concepts. Diffusion and elastic strain can be uncoupled fully, being a good approximation in many situations. We have used a correction to the stiffness of the rock under conditions of transverse isotropy and uniaxial strain to model borehole conditions. The concepts of phase, group, and energy velocities were analyzed to describe the location of the diffusion front, and the attenuation and quality factors were obtained to quantify the amplitude decay. We have found that the location of the front is described correctly by the energy velocity. The Green's function in anisotropic media can be obtained by applying a change of coordinates to the isotropic solution. We have simulated the diffusion in inhomogeneous media using a time-domain spectral explicit scheme and the staggered Fourier pseudospectral method to compute the spatial derivatives. The method is based on a spectral Chebychev expansion of the evolution operator of the system. The scheme allows the solution of linear periodic parabolic equations, having accuracy within the machine precision, in time and in space. The results match the analytic solution obtained from the Green's function. The performance of the algorithm is confirmed in the case of a pressure field generated by a fluid-injection source in a hydrocarbon reservoir where the properties vary fractally.

INTRODUCTION

Diffusion equations are obtained in poroelasticity and electromagnetism at low frequencies and under certain conditions, by which the inertial terms and displacement currents are neglected, respectively (e.g., Carcione, 2007). In hydrocarbon exploration and production, diffusion equations are used mainly to map subseafloor resistivity (e.g., Badea et al., 2001; Eidesmo et al., 2002) and to model fluid flow in reservoir rocks (Bear, 1988). Shapiro et al. (2002) describe the phenomenon of microseismicity caused by fluid injection in boreholes by using the diffusion equation obtained in the low-frequency limit of Biot's theory. Indeed, Chandler and Johnson (1981) show the equivalence between quasi-static fluid flow and Biot's diffusive wave (see also Carcione, 2007). Hence, fluid flow and pressure diffusion are phenomena described by the same differential equation.

Müller (2006) provides a detailed analysis of the pore pressure induced by a fluid-mass point source. Depending on the frequency content of the source function, different regimes can be identified, i.e., the diffusive regime in which only Biot's diffusive wave exists, and the propagation-diffusion regime in which slow and fast wave modes coexist. Müller (2006) shows that in the propagation-diffusion regime the induced pore pressure is reduced for most fluid-saturated rocks, and therefore the probability of triggering microearthquakes is reduced also. His results support the hypothesis that the diffusive slow P-wave is mainly responsible for the triggering of microearthquakes.

A convenient equation for anisotropic inhomogeneous media can be obtained from Biot's theory of poroelasticity. The diffusion can be uncoupled fully from the elastic deformations by neglecting the strain. A less stringent condition can be assumed by which we consider transverse isotropy and uniaxial strain conditions. Under these conditions, the effect of the elastic deformations requires the modification of the stiffness of the rock, involved in the diffusion equation. A plane-wave analysis provides the kinematic and dynamic quantities to interpret the physics of the diffusion, such as the phase, group, and energy velocities and the quality factor.

Existing schemes for numerical simulation of diffusion processes are based mostly on low-order finite-difference or finite-element methods (e.g., Chen, 2007) and therefore have low accuracy because of approximations of the time and space derivatives. In this work, we develop a fully spectral modeling method for the fluid-pressure diffusion problem in heterogeneous media. The algorithm uses an explicit scheme based on a Chebychev expansion of the evolution op-

Manuscript received by the Editor 29 December 2008; revised manuscript received 7 April 2009; published online 1 September 2009.
[1]Istituto Nazionale di Oceanografia e di Geofisica Sperimentale (OGS), Trieste, Italy. E-mail: jcarcione@inogs.it; dgei@ogs.trieste.it.

erator in the domain of the eigenvalues of the propagation matrix (Tal-Ezer, 1989; Carcione, 2007). The spatial derivatives are computed with the staggered Fourier pseudospectral method (Fornberg, 1996; Carcione, 2006). The algorithm has been used to solve the 1D telegraph equation for electric drill-string telemetry (Carcione and Poletto, 2003) and the electromagnetic diffusion equation (Carcione, 2006, 2007). The Chebychev method, either for parabolic or hyperbolic problems, has spectral accuracy in time and space and therefore avoids numerical dispersion, which is a characteristic feature of low-order schemes.

We model fractal inhomogeneities by using a von Kármán autocovariance probability function of high fractal dimension (von Kármán, 1948) applied to the spatial variations of the porosity. The permeability components and the stiffness are obtained by deterministic relations between these quantities and the porosity.

THE FLUID-PRESSURE DIFFUSION EQUATION

Diffusion equations are obtained in poroelasticity under certain conditions, by which the inertial terms are neglected. The quasi-static limit of Biot's poroelastic equations, to describe the diffusion of the second (slow) compressional mode, is obtained by neglecting the acceleration terms in the equations of momentum conservation and by considering the constitutive equations and Darcy's law (Biot, 1962).

Biot's classical equation

Biot's relevant stress-strain relation and Darcy's law for inhomogeneous media are given by

$$p = M(\zeta - \alpha_{ij}\epsilon_{ij}), \quad \zeta = -\partial_i w_i, \tag{1}$$

and

$$-\kappa_{ij}\partial_j p = -\kappa_{(i)}\partial_i p = \eta\partial_t w_i, \quad i = 1,\ldots,3 \tag{2}$$

(e.g., equations (8.399) and (8.401) in Carcione, 2007), where p is the fluid pressure, ζ is the variation of fluid content, w_i are the components of the fluid displacement vector relative to the solid, ϵ_{ij} are the components of the strain tensor of the skeleton (matrix), $\kappa_i = \kappa_{ij}\delta_{ij}$ are the components of the permeability tensor (in its principal system), η is the dynamic viscosity, α_{ij} are components of the effective-stress coefficient matrix (equation [7.139] in Carcione, 2007; see below), ∂_i is the spatial derivative with respect to the variable x_i, and ∂_t is the time derivative ($(x_1,x_2,x_3) = (x,y,z)$). The stiffness M is

$$M = \frac{K_s}{(1 - K/K_s) - \phi(1 - K_s/K_f)}, \tag{3}$$

where ϕ is the porosity, K_s is the bulk modulus of the solid grains, K_f is the fluid bulk modulus, and

$$K = \frac{1}{9}[c_{11} + c_{22} + c_{33} + 2(c_{12} + c_{13} + c_{23})], \tag{4}$$

with c_{IJ} the elastic constants of the (drained) skeleton. In many cases, M can be approximated by K_f/ϕ.

Combining equations 1 and 2 yields the diffusion equation

$$\frac{1}{M}\partial_t p + \alpha_{ij}\partial_t\epsilon_{ij} = \partial_i(a_i\partial_i p), \quad a_i = \frac{\kappa_i}{\eta}, \quad \text{and } i,j = 1,\ldots,3. \tag{5}$$

In the isotropic case, equation 5 becomes

$$\frac{1}{M}\partial_t p + \alpha\partial_t\epsilon_{ii} = \partial_i(a\partial_i p), \quad a = \frac{\kappa}{\eta}, \tag{6}$$

where $\alpha = 1 - K/K_s$, with K the bulk modulus of the skeleton.

Uncoupling fluid flow and deformation

The fluid pressure is coupled with the strain of the matrix in equations 5 and 6. This fact makes the problem much more difficult to solve, but there are situations in which these field variables can be uncoupled. They occur when the displacement field is irrotational or when the fluid is very compressible (e.g., Detournay and Cheng, 1993). We might avoid such approximation by using a less stringent one. The total stress is

$$\sigma_{ij} = c_{ijk\ell}\epsilon_{k\ell} - \alpha_{ij}p \tag{7}$$

(e.g., equation (7.132) in Carcione, 2007), where σ_{ij} are the components of the total stress tensor and $c_{ijk\ell}$ are the elastic constants in the four indices notation (Helbig, 1994).

Let us assume the case of a fluid-injection source in a borehole, transverse isotropy of the elastic and transport properties ($a_2 = a_1$), uniaxial strain conditions, and vertical deformations only. In this case, the only nonzero differential strain is $d\epsilon_{33}$. Assuming no changes in the vertical stress, we obtain from equation 7,

$$d\sigma_{33} = 0 \simeq c_{3333}d\epsilon_{33} - \alpha_{33}dp = c_{33}d\epsilon_{33} - \alpha_{33}dp. \tag{8}$$

Using this equation, equation 5 becomes

$$\partial_t p + s = M\Delta_I p, \tag{9}$$

where we have introduced a source term s,

$$\Delta_I = \partial_1(a_1\partial_1 p) + \partial_2(a_1\partial_2 p) + \partial_3(a_3\partial_3 p)$$
$$\text{and } \frac{1}{M} \to \frac{1}{M} + \frac{\alpha_{33}^2}{c_{33}}, \tag{10}$$

and the subindex I in the Laplacian indicates that it corresponds to inhomogeneous media; i.e., equation 9 is required when computing diffusion fields using direct methods (finite differences, finite elements, pseudospectral methods, and so on). The permeability tensor is diagonal with two independent components κ_1 and κ_3, so that

$$a_i = \frac{\kappa_i}{\eta}, \quad i = 1,3, \tag{11}$$

$$\alpha_{33} = 1 - (2c_{13} + c_{33})/(3K_s), \tag{12}$$

and M is given by equation 3, with

$$K = \frac{1}{9}[2c_{11} + c_{33} + 2(c_{12} + 2c_{13})]. \tag{13}$$

Another similar situation, although uncommon in a borehole, occurs when the strain tensor is isotropic, i.e., $d\epsilon_{11} = d\epsilon_{22} = d = 0$. It is easy to show that if $d\sigma_{33} = 0$, we obtain a stiffness

$M \to 1/[1/M + \alpha_{33}^2/(2c_{13} + c_{33})]$. Knowledge of M in both cases is useful to quantify the correction to be applied to the diffusion equation resulting from the deformation of the skeleton. More general approaches involving the coupling of fluid flow and deformation to take into account the coupled Biot's equations are given by Gutierrez and Lewis (2002).

If the medium is homogeneous, we can express equation 5 as

$$\partial_t p + s = \Delta_H p, \tag{14}$$

where

$$\Delta_H = b_1\partial_1^2 + b_2\partial_2^2 + b_3\partial_3^2, \quad b_i = Ma_i = M\frac{\kappa_i}{\eta},$$
$$i = 1,\ldots,3; \tag{15}$$

b_i are the principal components of the hydraulic diffusivity tensor, which can be defined only for homogeneous media. Otherwise, the Laplacian 10 has to be used for diffusion problems when the medium is heterogeneous.

PLANE-WAVE ANALYSIS

Let us assume a kernel of the form $\exp[\mathrm{i}(\omega t - \mathbf{k}\cdot\mathbf{x})]$, where ω is the angular frequency, $\mathbf{k}$ is the complex wavenumber vector, and $\mathbf{x}$ is the position vector. Assuming homogeneous fields, we have $\mathbf{k} = k(\ell_1,\ell_2,\ell_3)^{\mathsf{T}}$, where $k = \mathrm{Re}(k) - \mathrm{i}\alpha$, α is the attenuation factor, and ℓ_i are the direction cosines defining the propagation direction, where Re takes real part.

Dispersion relation and complex velocity

Substituting the above kernel into equation 14, in the absence of source, gives the dispersion equation

$$\mathrm{i}\omega = -(b_1\ell_1^2 + b_2\ell_2^2 + b_3\ell_3^2)k^2. \tag{16}$$

We define the complex velocity as

$$v_c = \frac{\omega}{k} = \sqrt{\mathrm{i}\omega(b_1\ell_1^2 + b_2\ell_2^2 + b_3\ell_3^2)}. \tag{17}$$

The same kinematic concepts used in wave propagation (acoustics and electromagnetism) are useful in this analysis (see Carcione, 2007, chapter 8).

Phase velocity, attenuation factor, and skin depth

The phase velocity and attenuation factor can be obtained from the complex velocity as

$$v_p = [\mathrm{Re}(v_c^{-1})]^{-1} \quad \text{and} \quad \alpha = -\omega\,\mathrm{Im}(v_c^{-1}), \tag{18}$$

respectively, where Im takes imaginary part. The skin depth is the distance d for which $\exp(-\alpha d) = 1/\mathrm{e}$, where e is Euler's number. It usually is taken as the effective distance of penetration of the signal. Then $d = 1/\alpha$; $d = \sqrt{2b/\omega}$ for isotropic media, where $b = \kappa M/\eta$. Using equation 17 yields

$$v_p = \sqrt{2\omega(b_1\ell_1^2 + b_2\ell_2^2 + b_3\ell_3^2)} \tag{19}$$

and

$$\alpha = \frac{1}{d} = \frac{\omega}{v_p}. \tag{20}$$

Envelope and group velocities

Without loss in generality, let us consider the (x,z)-plane, where $\ell_2 = 0$, $\ell_1 = \sin\theta$, $\ell_3 = \cos\theta$, and $\ell_1^2 + \ell_3^2 = 1$, where θ is the angle between the wavenumber vector and the z-axis. Carcione (1994, 2007) shows that the location of the wavefront in anisotropic attenuating media is given by the energy velocity because the concept of group velocity breaks down. Carcione also shows that the energy velocity can be approximated quite well by the envelope velocity, which is given by

$$v_{\mathrm{env}} = \sqrt{v_p^2 + \left(\frac{dv_p}{d\theta}\right)^2} \tag{21}$$

(equation (1.146) in Carcione, 2007). Using equation 19, we obtain

$$v_{\mathrm{env}} = v_p\frac{\sqrt{b_1^2\ell_1^2 + b_3^2\ell_3^2}}{(b_1\ell_1^2 + b_3\ell_3^2)^2} = \frac{2\omega}{v_p}\sqrt{b_1^2\ell_1^2 + b_3^2\ell_3^2}. \tag{22}$$

In the isotropic case, $b_1 = b_3$ and $v_{\mathrm{env}} = v_p$. We show below that the envelope velocity is exactly the energy velocity for equations of the form 14.

On the other hand, the components of the group velocity are equal to the derivative of the frequency ω with respect to the real wavenumber components, i.e., $\partial\omega/\partial\,\mathrm{Re}(k_i)$. The components are $k_i = k\ell_i$. The group-velocity vector can be obtained from the dispersion relation as

$$\mathbf{v}_g = -\left[\mathrm{Re}\left(\frac{\partial F/\partial\omega}{\partial F/\partial k_1}\right)\right]^{-1}\hat{\mathbf{e}}_1 - \left[\mathrm{Re}\left(\frac{\partial F/\partial\omega}{\partial F/\partial k_3}\right)\right]^{-1}\hat{\mathbf{e}}_3, \tag{23}$$

(equation (4.39) in Carcione, 2007), where, from equation 16,

$$F(k_1,k_3) = b_1k_1^2 + b_3k_3^2 + \mathrm{i}\omega = 0, \tag{24}$$

and $\hat{\mathbf{e}}_1$ and $\hat{\mathbf{e}}_3$ represent unit vectors in the x- and z-directions, respectively. Because $\mathrm{Im}(v_c) = v_p/2$, we obtain

$$\mathbf{v}_g = \frac{4\omega}{v_p}(b_1\ell_1\hat{\mathbf{e}}_1 + b_3\ell_3\hat{\mathbf{e}}_3) \tag{25}$$

and

$$v_g = \frac{4\omega}{v_p}\sqrt{b_1^2\ell_1^2 + b_3^2\ell_3^2} = 2v_{\mathrm{env}}. \tag{26}$$

In the isotropic case, we have $v_g = 2v_p$.

The group velocity obtained by Shapiro et al. (2002) differs from equation 26 in that the factor 4 is replaced by $\sqrt{8}$. Shapiro et al.'s approach is to compute the components $\partial\omega/\partial k_i$ and then take the absolute value of the result. (Note that $|v_c| = v_p/\sqrt{2}$.) Shapiro et al.'s velocity exceeds our energy (or envelope) velocity by a factor $\sqrt{2}$ (see next section). The problem of correctly defining the field velocities is important in many contexts, for instance, in inhomogeneous media containing random scatterers (Schriemer et al., 1997). When the scattering is strong, the propagation typically is very well described

using the diffusion approximation, and the group velocity generally differs from the energy velocity.

Energy velocity and wavefront

The calculation of the energy velocity requires establishment of the energy balance equation. Again, we use the fact that diffusion fields can be treated with the same mathematical formulation used for the propagation of waves. The energy balance could be developed explicitly, and the energy velocity can be obtained as the energy flux divided by the total energy. For brevity, we use an analogy between equation 5 and that describing propagation of seismic SH-waves (Carcione, 2007). The complex velocity of SH-waves, given by equation (4.106) in Carcione (2007), is mathematically equivalent to equation 17, provided that we make the following substitutions:

$$p_{66}\rightarrow \mathrm{i}\omega b_1, \quad p_{44}\rightarrow \mathrm{i}\omega b_3, \quad \rho\rightarrow 1, \tag{27}$$

where p_{66} and p_{44} are complex and frequency-dependent stiffnesses and ρ is the mass density. The energy velocity is given by equation (4.115) in Carcione (2007). Then, using this equation and the equivalence 27, we obtain

$$\mathbf{v}_e = \frac{2\omega}{v_{\mathrm{p}}}(b_1\ell_1\hat{\mathbf{e}}_1 + b_3\ell_3\hat{\mathbf{e}}_3). \tag{28}$$

As can be seen, by comparison to equation 22, $v_{\mathrm{env}} = v_e$. In the isotropic case, $b_1 = b_3$ and $v_e = v_{\mathrm{p}}$.

Equation 28 provides, in addition, the direction of the energy flux:

$$\tan\psi = \frac{b_1\ell_1}{b_3\ell_3} = \frac{\kappa_1}{\kappa_3}\tan\theta. \tag{29}$$

The velocity goes from zero at $\omega = 0$ to infinity at $\omega = \infty$. Hence, the definition of wavefront or diffusion front is related to a given frequency. We define the wavefront as the location of the tip of the energy velocity vector at unit propagation time.

Quality factor

The quality factor has two definitions in the literature, which give approximately the same value when $Q \gg 1$ (low-loss condition), as it is the case for seismic waves. These definitions are (1) Q_1 = twice the potential energy divided by the dissipated energy, and (2) Q_2 = the total energy divided by the dissipated energy. These are energy densities, time averaged over a cycle.

Here the low-loss condition does not hold. The first definition gives a quality factor

$$Q_1 = \frac{\mathrm{Re}(v_{\mathrm{c}}^2)}{\mathrm{Im}(v_{\mathrm{c}}^2)} = 0 \tag{30}$$

(see Carcione, 2007, equation (4.92)), where we use equation 17. The second definition gives

$$Q_2 = \frac{\mathrm{Re}^2(v_{\mathrm{c}})}{\mathrm{Im}(v_{\mathrm{c}}^2)} = \frac{1}{2} \tag{31}$$

(see Carcione, 2007, equation (8.305)). Because a pure diffusion process does not store the energy, which is completely dissipated, Q_1 seems to be more representative of the physics. This can be viewed in terms of mechanical models. It is well known that a dashpot represents a diffusion equation and that this element dissipates all the energy without any storage.

GREEN'S FUNCTION

Here, we obtain the response of the medium to a time impulse. The following change of coordinates,

$$x\rightarrow x'\sqrt{b_1}, \quad y\rightarrow y'\sqrt{b_2}, \quad z\rightarrow z'\sqrt{b_3}, \tag{32}$$

transforms Δ_H in equation 14 into a pure Laplacian differential operator. Using equation 32, equation 14 for the Green's function is

$$\partial_t G - \Delta' G = \delta(r')\delta(t), \tag{33}$$

where δ is Dirac's function, and

$$\Delta' = \partial_{1'}^2 + \partial_{2'}^2 + \partial_{3'}^2. \tag{34}$$

Its solution is

$$G = \frac{1}{(4\pi t)^{n/2}}\exp[-r'^2/(4t)]H(t) \tag{35}$$

(e.g., Carslaw and Jaeger, 1984), where n is the space dimension and

$$r' = \sqrt{\frac{x^2}{b_1} + \frac{y^2}{b_2} + \frac{z^2}{b_3}} \tag{36}$$

(omit the y-term if $n = 2$). The diffusion-length vector (ℓ_1,ℓ_2,ℓ_3) is defined as $r' = \sqrt{4t}$. It is obtained from

$$\frac{\ell_1^2}{b_1} + \frac{\ell_2^2}{b_2} + \frac{\ell_3^2}{b_3} = 4t. \tag{37}$$

It is a measure of how far the field has propagated at time t.

Having the Green's function, one can compute the solution for a source time history $s(t)$ as

$$p = G * s. \tag{38}$$

The spectrum of function $s(t)$ should be significant in a frequency range when the assumption of quasi-static poroelasticity is valid (Müller, 2006).

In particular, for $s = H$ (uniform injection rate), we have for the 3D diffusion case 35

$$p = \frac{1}{(4\pi)^{3/2}}\int_0^t \frac{1}{\tau^{3/2}}\exp(-r'^2/4\tau)d\tau = \frac{1}{4\pi r'}\,\mathrm{erfc}\left(\frac{r'}{\sqrt{4t}}\right), \tag{39}$$

where "erfc" is the complementary error function; $\mathrm{erfc}(q) = 1 - \mathrm{erf}(q) = (2/\sqrt{\pi})\int_q^\infty \exp(-p^2)dp$, where "erf" is the error function.

FRACTAL MEDIA

We vary the porosity fractally and compute the permeability components and elastic moduli from deterministic relations between these quantities and the porosity. This model contains characteristics of realistic heterogeneous media.

Let $\Delta\phi_m$ be the maximum deviation of the porosity from the background value ϕ_0. The porosity at (x,y,z) is subjected first to the variations $(\Delta\phi)^r$, so that

$$-\Delta\phi_m \le (\Delta\phi)^r \le \Delta\phi_m, \tag{40}$$

where $(\Delta\phi)^r$ is obtained from a random generator, and the superindex r denotes random. (Random numbers between 0 and 1 are generated and then scaled to the interval $[-1,1]\Delta\phi_m$.)

Small-scale porosity variations in the reservoir can be described by the von Kármán autocovariance function. This function contains characteristics seen in models of heterogeneity in sedimentary rocks. It describes self-similar and self-affine media rich in short-wavelength components, providing a fractal spatial description of a fabric over a wide-scale range. The exponential function is a particular case of this autocovariance function, which is used widely in seismic applications (e.g., Dolan and Bean, 1997). Alternative choices are given, for instance, in Molz et al. (2004).

The corresponding wavenumber-domain power spectrum of the von Kármán function is

$$P(k_1,k_2,k_3) = C(1 + k^2\ell^2)^{-(\nu+n/2)}, \tag{41}$$

where $k = \sqrt{k_1^2 + k_2^2 + k_3^2}$ is the wavenumber, ℓ is the correlation length, $\nu (0 < \nu < 1)$ is a self-similarity coefficient, C is a normalization constant, and n is the Euclidean dimension. The von Kármán correlation function describes self-affine, fractal processes of fractal dimension $n + 1 - \nu$ at scales smaller than ℓ.

The porosity then is calculated as

$$\phi(x,y,z) = \phi_0 \pm \Delta\phi(x,y,z), \tag{42}$$

where

$$\widetilde{\Delta\phi}(k_1,k_2,k_3) = \widetilde{(\Delta\phi)}^r(k_1,k_2,k_3)P(k_1,k_2,k_3), \tag{43}$$

with $\widetilde{(\Delta\phi)}^r(k_1,k_2,k_3)$ being the Fourier transform of $(\Delta\phi)^r(x,y,z)$. (The tilde denotes the space Fourier transform.)

Porosity and permeability are related by the Kozeny-Carman relation (Mavko et al., 1998). Let us assume

$$\kappa_3 = \frac{B\phi^3 D^2}{(1-\phi)^2}, \tag{44}$$

where D is the grain diameter and B is a dimensionless constant ($B = 0.003$ in our calculations).

We use the model of Krief et al. (1990) to obtain the dry-rock modulus K. The porosity dependence is consistent with the concept of critical porosity because the moduli should be small above a certain value of the porosity (usually from 0.4 to 0.6). The modulus is given by

$$K = K_s(1-\phi)^{A/(1-\phi)}, \tag{45}$$

where A is a constant that depends on the rock type. We have replaced equation 4 by the approximation 45. Note that the diffusion process is controlled mainly by the permeability tensor components, which might be very different in different directions (in contrast to the elastic moduli).

The numerical algorithm for solving the diffusion equations is given in detail in Appendix A.

PHYSICS AND SIMULATIONS

To illustrate the physics in homogeneous media, we use the following material properties: $c_{11} = 35$ GPa, $c_{12} = 3$ GPa, $c_{13} = 5$ GPa, $c_{33} = 25$ GPa, $K_s = 40$ GPa, $K_f = 2.25$ GPa, $\phi = 0.25$, $\kappa_1 = 200$ mD, $\kappa_3 = 50$ mD, and $\eta = 1$ cP. Figure 1 shows the phase and energy velocities as a function of the propagation angle. The frequency is 0.001 Hz. At $\theta = 0$, we have propagation along the z-direction where the permeability is minimum. Thus, the velocities also have a minimum along this direction. Figure 2 shows a snapshot of the pressure field at $t = 4$ hr 30 min. The 2D image in Figure 2a shows the anisotropic features of the diffusion. A blowup along a horizontal line passing through the source is shown in Figure 2b. Here and in the following plots, the field is normalized with respect to its maximum value. The arrow indicates the wavefront, which has been calculated with the energy velocity 28 along the direction of maximum permeability, i.e., 240 m/hr (see Figure 1).

We now compare the numerical and analytic solutions in homogeneous media. To compute the transient responses, we use as a source a Ricker time history of the form

$$h(t) = \left(a - \frac{1}{2}\right)\exp(-a), \quad a = \left[\frac{\pi(t-t_s)}{t_p}\right]^2, \tag{46}$$

where t_p is the period of the wave (the distance between the side peaks is $\sqrt{6}t_p/\pi$), and we take $t_s = 1.4t_p$. Its frequency spectrum is

$$H(\omega) = \left(\frac{t_p}{\sqrt{\pi}}\right)\bar{a}\exp(-\bar{a} - i\omega t_s), \quad \bar{a} = \left(\frac{\omega}{\omega_p}\right)^2,$$

$$\omega_p = \frac{2\pi}{t_p}. \tag{47}$$

The peak frequency is $f_p = 1/t_p$.

For the comparison, we take $f_p = 0.001$ Hz, corresponding to a period of approximately half an hour. We consider the same properties indicated above, $n = 2$ (2D space), and a mesh with grid points $N_x = N_z = 273$, and $\Delta_x = \Delta_z = 10$ m. The first time step is $dt = 2$ hr and 15 min, greater than the duration of the source (nearly $2t_s$ or approximately 1 hr and 33 min). Then we use the obtained solution as

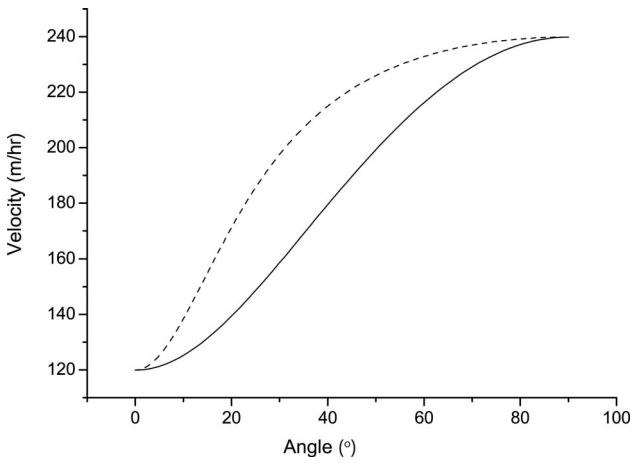

Figure 1. Phase and energy velocities (solid and dashed lines) as a function of the propagation angle.

an initial condition and propagate the field with 10 time steps of duration dt each. The solutions are computed at $x = z = 300$ m. Figure 3 shows the comparison, in which the solid lines correspond to the analytic solutions, the empty circles to the anisotropic case, and the black circles to the isotropic case ($\kappa_1 = \kappa_3 = 50$ mD). As can be seen, the agreement is excellent.

The simulation in heterogeneous media considers a low-frequency source with a peak frequency $f_p = 0.03$ Hz. The rock is modeled as a fractal medium described by $\phi_0 = 0.35$, $\Delta\phi_m = 0.15$, $\ell = 20$ m, $\nu = 0.18$, and $n = 2$. We assume $D = 0.25$ mm, $\kappa_1 = 4\kappa_3$, $\eta = 1$ cP, $K_s = 40$ GPa, $\mu_s = 38$ GPa, $A = 5.13$, $K_f = 2.61$ GPa, and $\rho_f = 1032$ kg/m^3; $K = 1.33$ GPa is obtained from equation 45. If we assume a dry-rock shear modulus $\mu = 0.67K\mu_s/K_s$, we obtain the average P- and S-wave velocities 2061 and 643 m/s, respectively, and an average density of 2050 kg/m^3. The average vertical permeability is $\kappa_3 = 1.9$ D, with minimum and maximum permeabilities of 0.25 D and 9.25 D. The average value of M is 3.6 GPa, and the average field velocities along the vertical and horizontal directions are 4130 and 8270 m/hr, respectively.

Figure 4 shows a map of the vertical permeability. To perform the simulation, we use the same grid of the previous simulation. The first time step is $dt = 135$ s, greater than the duration of the source (93 s). Then five time steps of 135 s are used to compute the snapshot and time history shown in Figures 5 and 6, respectively. The last figure shows a comparison of the pressure corresponding to the average and fractal media (solid line and symbols, respectively), where the average properties are $M = 3.6$ GPa, $\kappa_1 = 7.6$ D, and $\kappa_3 = 1.9$ D. The difference of the peak values is nearly 15%, a difference that can be important in real applications. Note that in this work we are simulating pore-pressure diffusion (i.e., diffusion of the slow

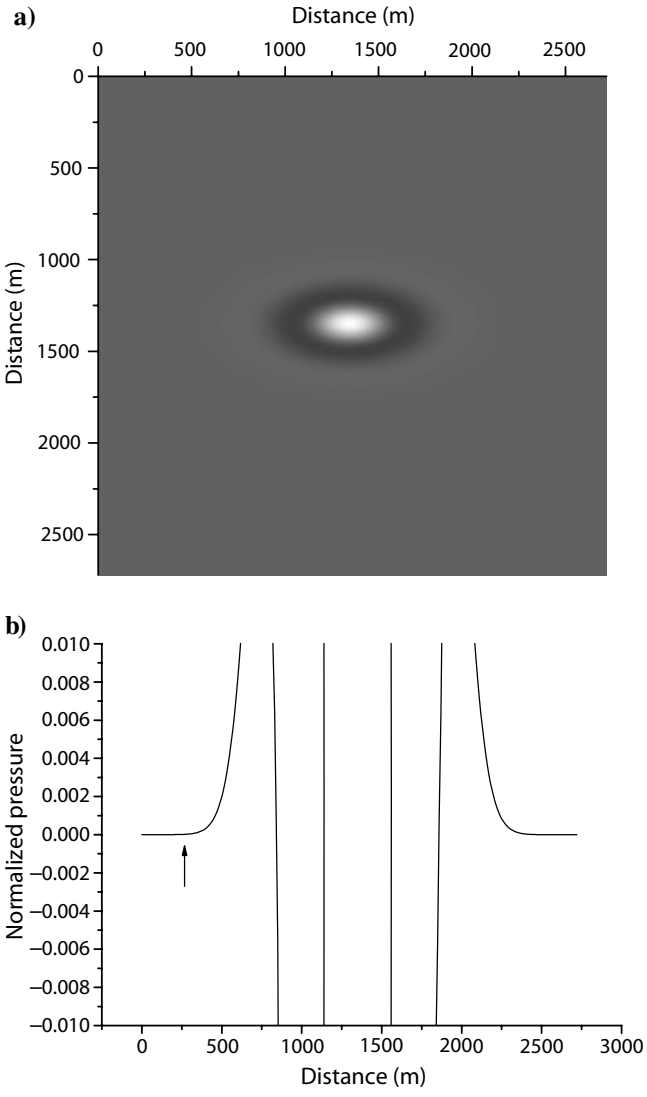

Figure 2. Snapshot of the pressure field at $t = 4$ hr 30 min. (a) 2D image; (b) 1D image (blowup) along a horizontal line passing through the source and the direction of maximum permeability. The arrow in (b) indicates the location of the wavefront computed with the energy velocity 28 at $\theta = \pi/2$ or $\ell_1 = 1$.

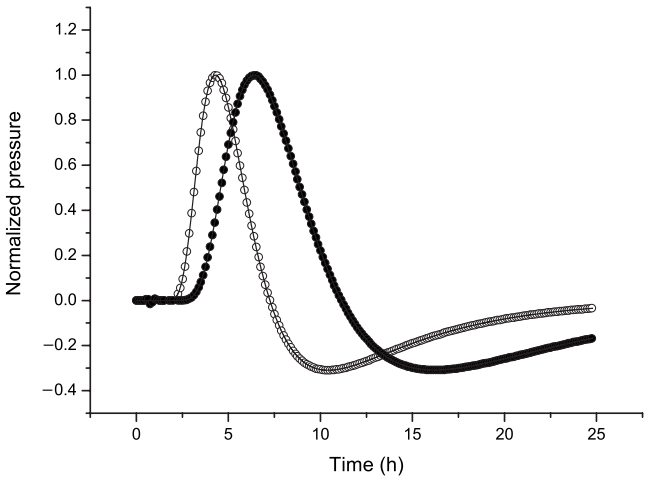

Figure 3. Comparison between the analytic (solid lines) and numerical solutions at 424 m from the source location. The open and solid circles correspond to the anisotropic and isotropic cases, respectively. Both fields are normalized to one, but the maximum in the former case is twice the maximum of the latter case.

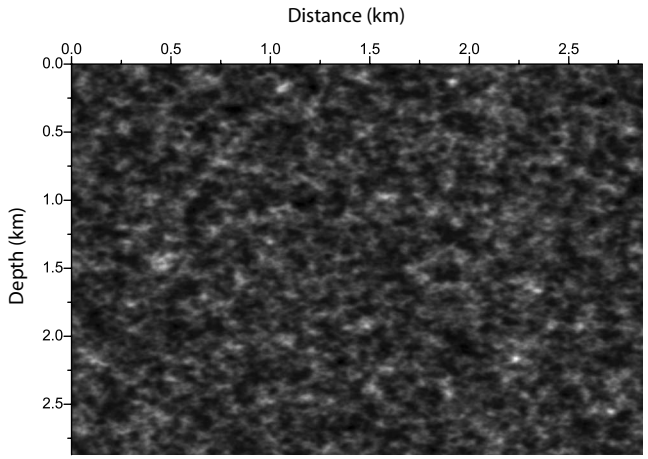

Figure 4. Fractal image of the vertical permeability κ_3 corresponding to a typical high-porosity sandstone. The average size of the heterogeneities is 20 m.

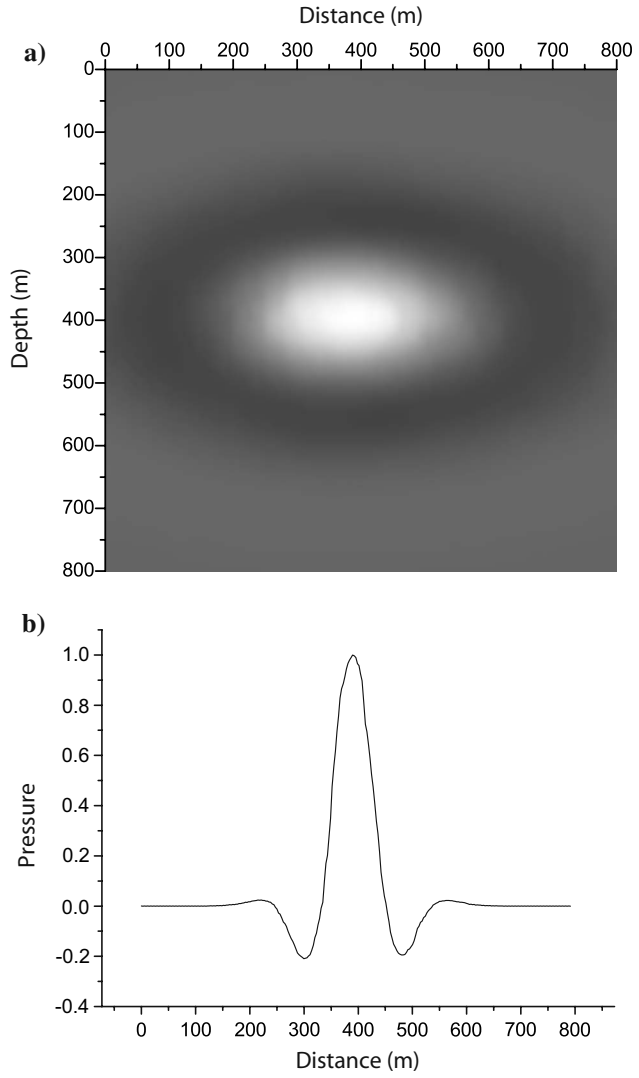

Figure 5. A 2D snapshot of the pressure field in the fractal medium (a) at 810 s and horizontal section (b) through the source location.

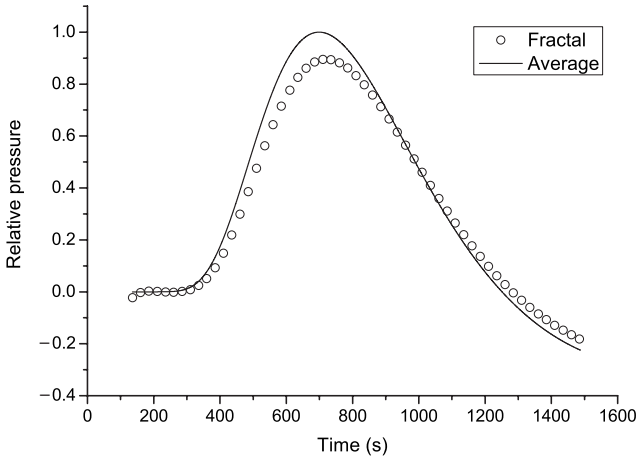

Figure 6. Comparison between the pressure in the average homogeneous medium (solid line) and the pressure in the fractal medium (circles), at 424 m from the source location.

Biot mode) rather than mass flow. Although the equations are equivalent, the effect of gravity has to be included in the equations in the latter case, when modeling flow through vertical extensions such as the medium given in Figure 4.

CONCLUSIONS

We have formulated a theory for fluid-pressure diffusion in inhomogeneous anisotropic media. The coupling between the pressure and deformation of the frame is taken into account for the case of uniaxial strain conditions. The approximation involves a modification of the stiffness. The physical quantities have been obtained by using a plane-wave kernel and concepts from wave propagation in anelastic media. In particular, we show that the envelope velocity (a kinematic quantity) is equal to the energy velocity (a dynamic quantity). This is not the case for waves. Our group velocity is twice the energy velocity and is greater than a previous definition of group velocity by a factor $\sqrt{2}$. The relation between the energy angle and the phase angle depends on the ratio between the horizontal and vertical permeabilities, and therefore strong differences are expected between the flux and wave-vector directions, compared to the seismic (propagation) case. Using the seismic definition of quality factor, we obtain a zero value, which is more physical than the accepted value of one half. This new implications are useful to track the diffusion front in reservoir rocks, where the signal travels at the energy velocity, as shown by the time response. We have obtained also the time-domain Green's function in homogeneous media.

Simulation of pressure diffusion in inhomogeneous media has been achieved by using a time-domain spectral method, which has high temporal accuracy and allows us the use of a coarse numerical mesh. The algorithm has been tested with the Green's function and applied to pressure diffusion in fractal permeability media, simulating realistic reservoir conditions.

ACKNOWLEDGMENTS

We thank the editor Boris Gurevich and anonymous reviewers for many useful comments.

APPENDIX A

THE NUMERICAL ALGORITHM

Equation 9 has the form

$$\partial_t p + s = Gp, \tag{A-1}$$

where

$$G = M(\partial_1 a_1 \partial_1 + \partial_2 a_2 \partial_2 + \partial_3 a_3 \partial_3) \tag{A-2}$$

is the propagation operator containing the spatial derivatives and material properties. Considering a discretization with N number of grid points, equation A-1 becomes a system of N ordinary differential equations at the grid points. The solution to equation A-1, subject to the initial condition $p(0) = p_0$, is given by

$$p_N(t) = \exp(tG_N)p_N^0 + \int_0^t \exp(\tau G_N)s_N(t-\tau)d\tau, \tag{A-3}$$

where p_N^0 is the initial-condition field vector, $\exp(tG_N)$ is called evolution operator, and the subindex N indicates that those quantities are discrete representations of the respective continuous quantities. We consider a separable source term $s = a_N h(t)$, where a_N is the spatial distribution of the source and the function $h(t)$ is the source time history. A fully discrete solution of equation A-3 is achieved by approximating the evolution operator. For instance, if there is no source, the solution can be expressed by

$$p_N(t) = H_m(tG_N)p_N^0, \tag{A-4}$$

where H_m is a polynomial of degree m that converges to $\exp(tG_N)$ in the domain that includes all the eigenvalues of the operator tG_N.

To solve equation A-3, we use a time-integration technique based on the Chebychev expansion of the function $\exp(u)$ (Tal-Ezer, 1989; Carcione, 2006). Let

$$v = \frac{1}{et}(u + et), \quad -1 \le v \le 1, \tag{A-5}$$

where e is the absolute value of the maximum eigenvalue of matrix G_N. As we see below, the eigenvalues are close to the real axis, and their real part is negative. Using equation A-5, we have

$$\exp(u) = \exp(-et)\exp(etv) = \sum_{k=0}^{\infty} e_k T_k(v), \tag{A-6}$$

where $T_k(v)$ is the Chebychev polynomial of order k, and

$$e_k = c_k \exp(-et) I_k(et) \tag{A-7}$$

for initial conditions without source, and

$$e_k = c_k \int_0^t \exp(-e\tau) I_k(e\tau) h(t-\tau) d\tau \tag{A-8}$$

in the presence of source without initial conditions

$$c_k = \begin{cases} 1, & k = 0, \\ 2, & k \ge 1, \end{cases} \tag{A-9}$$

and I_k is the modified Bessel function of order k. Thus, the m degree polynomial approximation of $\exp(u)$ is

$$H_m(u) = \sum_{k=0}^{m} e_k T_k(v(u)). \tag{A-10}$$

Because of equation A-5, we substitute the operator F_N defined as

$$F_N = \frac{1}{e}(G_N + e), \tag{A-11}$$

for v. For instance, in the absence of sources, the fully discrete solution is

$$p_N^m = \sum_{k=0}^{m} e_k T_k(F_N) p_N^0. \tag{A-12}$$

The expression $T_k(F_N)p_N^0$ is computed by using the recurrence relation

$$T_k(u) = 2uT_{k-1}(u) - T_{k-2}(u), \quad k \ge 2, \tag{A-13}$$

$$T_0(u) = 1, \quad T_1(u) = u. \tag{A-14}$$

Hence,

$$T_k(F_N)p_N^0 = 2F_N T_{k-1}(F_N)p_N^0 - T_{k-2}(F_N)p_N^0, \quad k \ge 2, \tag{A-15}$$

$$T_0(F_N)p_N^0 = p_N^0, \quad T_1(F_N)p_N^0 = F_N p_N^0. \tag{A-16}$$

The algorithm is a three-level scheme because it uses the recurrence relation. The first time step should be larger than the duration of the source. Results at small time steps to compute time histories at specified points of the grid do not require significant additional computational effort. A slight modification of equation A-12 can be used:

$$p_N^m(t') = \sum_{k=0}^{m} e_k(t') T_k(F_N) p_N^0, \tag{A-17}$$

for $t < t'$. This calculation does not require significantly more computations because the terms involving the spatial derivatives $T_k(F_N)p_N^0$ do not depend on the time variable and are calculated in any case. Only the coefficients e_k are time dependent, so that additional sets of Bessel functions need to be computed.

Accuracy and stability were investigated by Tal-Ezer (1989), who shows that the algorithm is much more efficient than a modified Euler scheme (see below).

Maximum eigenvalue

Let us consider the homogeneous case and equation 15. In the Fourier method, the second derivative is replaced by $-k_i^2$, where k_i is the wavenumber. The maximum wavenumber is the Nyquist wavenumber, which for grid spacing Δx is $\pi/\Delta x$. Hence, the maximum eigenvalue e is

$$e = -\pi^2\left(\frac{b_1}{\Delta x^2} + \frac{b_2}{\Delta y^2} + \frac{b_3}{\Delta z^2}\right). \tag{A-18}$$

Note that e takes real negative values. As Tal-Ezer (1989) shows, the polynomial degree m should be of the order of $\sqrt{et}$.

Spatial differentiation

The algorithm uses the staggered Fourier method, which consists of a spatial discretization and calculation of spatial derivatives using the fast Fourier transform (Fornberg, 1996; Carcione, 2007). Staggered operators evaluate derivatives between grid points. For instance, if k_1 is the wavenumber component, a phase shift $\exp(\pm \mathrm{i} k_1 \Delta x/2)$ is applied when computing the x-derivative, where $\mathrm{i} = \sqrt{-1}$. Then $\partial_1 a_1 \partial_1$ is calculated as $D_1^- a_1 D_1^+$, where $D_1^\pm$ is the discrete operator and $\pm$ refers to the sign of the phase shift. The spatial differentiation requires the interpolation of the material properties at half grid points.

Accuracy and efficiency

The present algorithm has infinite accuracy in time and in space, and is highly efficient because the stability condition requires a time step $\Delta t = O(1/N)$ compared to $\Delta t = O(1/N^2)$ for finite-order explicit schemes. Moreover, the error in time decays exponentially. Tal-Ezer carries out an error and stability analysis for the equation $\partial_t U - G\partial_1^2 U = 0$, where $G = 1$ and $N = 64$. If m indicates the minimum number of applications of the operator $tF_N U_N$, Tal-Ezer shows that the Chebychev method requires $m = 96$ to be stable against $m = 768$ for a modified Euler scheme. Regarding accuracy, he obtains $m = 70$ (present method) versus $m = 20{,}000$ (Euler method) for $N = 32$, $t = 1$, and an ℓ_2-error equal to 10^{-6}. The last test involves a variable coefficient problem with $G = a(x)\partial_1^2 + b(x)\partial_1 + c(x)$. An ℓ_2-error less than 10^{-8} requires $m = 100$ (present method) versus $m = 480$ (Euler method) for $N = 64$ and $t = 1$. Despite the 1D character of the equations, these verifications are general regarding the dimensionality of the space because the spatial derivatives are performed by the pseudospectral Fourier method, which has been used widely and tested for hyperbolic equations (Tal-Ezer, 1986).

Absorbing boundaries

The boundaries of the mesh might produce wraparounds caused by the periodic properties of the Fourier method. By analogy with the wave equation, the algorithm uses the classical damping approach for hyperbolic problems to avoid these nonphysical artifacts (Kosloff and Kosloff, 1986; Carcione, 2007). The method is simply to modify the propagation operator $G \rightarrow G - \gamma$ in the absorbing strips around the mesh, where γ is the absorbing parameter.

REFERENCES

Badea, E. A., M. E. Everett, G. A. Newman, and O. Biro, 2001, Finite-element analysis of controlled-source electromagnetic induction using Coulomb-gauged potentials: Geophysics, **66**, 786–799.

Bear, J., 1988, Dynamics of fluid flow in porous media: Dover Publications.

Biot, M. A., 1962, Mechanics of deformation and acoustic propagation in porous media: Journal of Applied Physics, **33**, 1482–1498.

Carcione, J. M., 1994, Wavefronts in dissipative anisotropic media: Geophysics, **59**, 644–657.

———, 2006, A spectral numerical method for electromagnetic diffusion: Geophysics, **71**, no. 1, I1–I9.

———, 2007, Wave fields in real media: Theory and numerical simulation of wave propagation in anisotropic, anelastic, porous and electromagnetic media: Elsevier.

Carcione, J. M., and F. Poletto, 2003, Electric drill-string telemetry: Journal of Computational Physics, **186**, 596–609.

Carslaw, H. S., and J. C. Jaeger, 1984, Conduction of heat in solids: Clarendon Press.

Chandler, R. N., and D. L. Johnson, 1981, The equivalence of quasi-static flow in fluid-saturated porous media and Biot's slow wave in the limit of zero frequency: Journal of Applied Physics, **52**, 3391–3395.

Chen, Z., 2007, Reservoir simulation: Mathematical techniques in oil recovery: Society for Industrial and Applied Mathematics (SIAM).

Detournay, E., and A. H.-D. Cheng, 1993, Fundamentals of poroelasticity, *in* C. Fairhurst, ed., Comprehensive rock engineering: Principles, practice and projects, volume, 2, chapter 5: Pergamon, 113–171.

Dolan, S. S., and C. J. Bean, 1997, Some remarks on the estimation of fractal scaling parameters from borehole wire-line logs: Geophysical Research Letters, **24**, 1271–1274.

Eidesmo, T., S. Ellingsrud, L. M. MacGregor, S. Constable, M. C. Sinha, S. Johansen, F. N. Kong, and H. Westerdahl, 2002, Sea bed logging (SBL), a new method for remote and direct identification of hydrocarbon filled layers in deepwater areas: First Break, **20**, 144–151.

Fornberg, B., 1996, A practical guide to pseudospectral methods: Cambridge University Press.

Gutierrez, M. S., and R. W. Lewis, 2002, Coupling of fluid flow and deformation in underground formations: Journal of Engineering Mechanics, **128**, 779–787.

Helbig, K., 1994, Foundations of anisotropy for exploration seismics: Pergamon Press.

Kosloff, R., and D. Kosloff, 1986, Absorbing boundaries for wave propagation problems: Journal of Computational Physics, **63**, 363–376.

Krief, M., J. Garat, J. Stellingwerff, and J. Ventre, 1990, A petrophysical interpretation using the velocities of P and S waves (full waveform sonic): The Log Analyst, **31**, 355–369.

Mavko, G., T. Mukerji, and J. Dvorkin, 1998, The rock physics handbook: Tools for seismic analysis in porous media: Cambridge University Press.

Molz, F. J., H. Rajaram, and S. Lu, 2004, Stochastic fractal-based models of heterogeneity in subsurface hydrology: Origins, applications, limitations, and future research questions: Reviews of Geophysics, **42**, RG1002, doi: 10.1029/2003RG000126.

Müller, T. M., 2006, Spatiotemporal pore pressure evolution due to fluid-mass point sources in dynamic poroelasticity: Geophysical Journal International, **165**, 906–912.

Schriemer, H. P., M. L. Cowan, J. H. Page, P. Sheng, Z. Liu, and D. A. Weitz, 1997, Energy velocity of diffusing waves in strongly scattering media: Physical Review Letters, **79**, 3166–3169.

Shapiro, S. A., E. Rothert, V. Rath, and J. Rindschwentner, 2002, Characterization of fluid transport properties of reservoirs using induced microseismicity: Geophysics, **67**, 212–220.

Tal-Ezer, H., 1986, Spectral methods in time for hyperbolic problems: SIAM Journal of Numerical Analysis, **23**, 11–26.

———, 1989, Spectral methods in time for parabolic problems: SIAM Journal of Numerical Analysis, **26**, 1–11.

von Kármán, T., 1948, Progress in the statistical theory of turbulence: Journal of Marine Research, **7**, 252–264.